nature communications

Article

https://doi.org/10.1038/s41467-024-54929-0

Observation of edge bound states in the continuum at truncated silicon pillar photonic crystal

Received: 20 June 2024

Accepted: 26 November 2024

Published online: 04 December 2024

Check for updates

Rodrigo Sato[1], Christian Vinther Bertelsen[2], Maxim Nikitin[1], Elena Lopez Aymerich[3], Radu Malureanu[1], Winnie Edith Svendsen[2], Andrei V. Lavrinenko[1] & Osamu Takayama[1]

Bound states in the continuum are optical modes with extremely high-quality factors and narrow resonances, which exist in the dispersion spectrum of the radiative region above the light line. A unique bound state in the continuum is supported at the edge of truncated photonic crystals, which is a type of a Fabry-Pérot type bound state in the continuum, but has never been observed in experiments. Here, we demonstrate the bound states in the continuum supported at the edge array of silicon (Si) pillars whose diameter is bigger than that of the rest of a Si-pillar two-dimensional photonic crystal. We also show the tunability of the resonance and surface sensitivity of the mode when Si pillars are conformally coated with nanometer-thick aluminium oxide films. The presence of an oxide nanofilm improves the quality factor by over 60 % and shifts the resonance wavelength. Such behavior signifies the substantial potential of the bound states in the continuum on two-dimensional photonic crystals for post-fabrication tuning of the quality factor and surface sensing applications.

Optical bound state in the continuum (BIC) is a highly localized optical mode trapped in a structure in a lossless regime regardless of the presence of a leakage channel due to the radiation feature dictated by the dispersion spectrum[1–6]. A BIC mode occurs at a certain special point of the dispersion diagram as a result of the destructive interference in the host structure that suppresses the radiative mode. Hence, light is trapped within the structure while otherwise, it should leak out. The unique feature of BIC is its very narrow resonance, in other words, an extremely high quality (Q) factor, theoretically reaching infinitely high numbers in the case of an ideal structure with an infinite lattice, absence of material absorption, and structural defects. In a realistic experimental system with a finite number of periodic elements and such imperfections as surface roughness and material loss, a BIC is called a quasi-BIC, which possesses a high but finite Q-factor. Intentionally introduced perturbation of structures also allows for the control of the Q-factor. High Q-factors and highly confined electric fields of BIC modes are attractive for various potential applications, such as lasing[7,8], enhancement of the second- and third-harmonic generation[9–15], light modulation[16], biochemical sensing[17–27] and imaging[28], upconversion[29].

Up to present, BIC modes have been observed in various periodic systems, including arrays of dielectric pillars[2] and grating structures[30], metasurfaces in various designs[7–20,23,25,31–33], as well as aperiodic systems including a single resonator[22], anisotropic waveguides[34] and interfaces[35]. Furthermore, photonic crystal (PhC) structures are other settings where BIC modes are conventionally observed[3,17,21,28,29]. A photonic crystal is a periodic arrangement of dielectric or metallic elements with a period typically smaller than the wavelength of light.

[1]DTU Electro, Technical University of Denmark, Ørsteds Plads, Building 343, DK-2800 Kgs. Lyngby, Denmark. [2]DTU Bioengineering – Department of Biotechnology and Biomedicine, Technical University of Denmark, Søltofts Plads, Building 221, DK-2800 Kgs. Lyngby, Denmark. [3]DTU Nanolab - National Centre for Nano Fabrication and Characterization, Technical University of Denmark, Ørsteds Plads, Building 347, DK-2800 Kgs. Lyngby, Denmark.
e-mail: otak@dtu.dk

A characteristic feature of a PhC is the presence of a wavelength interval where light propagation is prohibited, referred to as a photonic bandgap (or a stop band)[36]. A two-dimensional photonic crystal (2DPhC) is typically an air hole array in a dielectric matrix or an array of dielectric discs or pillars erected on a substrate in an air background. Among other configurations, quasi-BIC modes in 2DPhCs have been observed in a square-lattice air hole array in a silicon nitride slab[3,17], flower pattern in a Si slab[37], and Si discs in square lattice structures[38].

Two major types of BIC modes are supported on PhC structures: symmetry-protected (SP) BICs and accidental BICs[4]. SP-BICs exist at the Γ point of the dispersion diagram and do not possess in-plane wavevector components. On the other hand, accidental BICs, which are also referred to as Fredrich-Wintgen bound states in the continuum (FW-BIC), possess a non-zero in-plane wavevector and thus are propagating along the structure. FW-BICs have been observed in 2DPhC systems[3,21,28,29,37]. However, apart from these two major types, a unique type of a BIC surface mode has been predicted, which is supported at the edge of a truncated 2DPhC. To host such a mode, the terminating row of dielectric pillars should have a different diameter from the rest of the pillars[39,40]. Depending on the pillar diameter, either BIC modes that exist above light line or surface modes below the light line can be supported. The predicted BIC modes are Bloch surface-localized eigenstates, discrete states supported at the edge periodic arrangement, such as photonic crystals and gratings, which exist inside the free space continuum above the light line. While such modes leak into free space, under certain conditions, the incoming and back-reflected leakage radiation interfere destructively and result in no leakage. Initially, the predicted BICs are called Bloch BIC. Other Bloch BICs have been studied for 1D gratings[41,42]. In order to distinguish from these Bloch BIC on 1D gratings and surface modes at the edge of 2DPhC, we refer the current BIC under investigation as "edge BICs" in this article.

An edge BIC mode is also categorized as a Fabry-Pérot (FP) type BIC[4,5] that is trapped between two reflectors. FP-BICs were theoretically studied for systems where reflectors are an asymmetric ridge with different thickness of waveguide films[43] or anisotropic one-dimensional PhC[44]. Some of them have been experimentally observed for an array of dielectric waveguides where the reflectors are waveguide array and isotropic dielectric media[45] and a metasurface made of gold nanoparticles, where a gold film above the metasurface is used as a reflector[16]. In the case of FP-BICs supported in 2DPhCs, the terminating layer of larger Si pillars is sandwiched between a pair of reflective interfaces, namely, the interface with air and that of 2DPhC with a photonic bandgap as the reflector[39,40]. Here, the air forms a leakage channel. FP-BIC modes with an electric field parallel to the pillars (TM polarization) exist within the photonic bandgap of the 2DPhC. As a result, the BIC mode propagates along the terminating array of dielectric pillars, being highly localized in their vicinity. Here we also stress that FP-BICs exist within the photonic bandgap above the light line, distinguishing them from FW-BICs, which are associated with one of the propagating modes of the 2DPhC outside the photonic bandgap[3,21,28,29,37].

Here, we experimentally demonstrate the special type of Fabry-Pérot bound states in the continuum for near-infrared wavelengths supported at the edge of a two-dimensional photonic crystal patch. The 2DPhC is composed of Si pillars in a square lattice arrangement. One edge of 2DPhC structures is truncated by an array of Si pillars whose diameter is bigger than the rest of the pillars, as shown in Fig. 1a – c. We refer to this particular quasi-BIC mode as edge BIC, which distinguishes from other types of observed FP-BICs[45] and surface BIC supported at the interface of anisotropic media[35]. The quality factor and resonance wavelength of the edge BIC modes are changed by a slight change in the terminating layer diameter by even a few nanometers. To the best of our knowledge, this is the first report on the

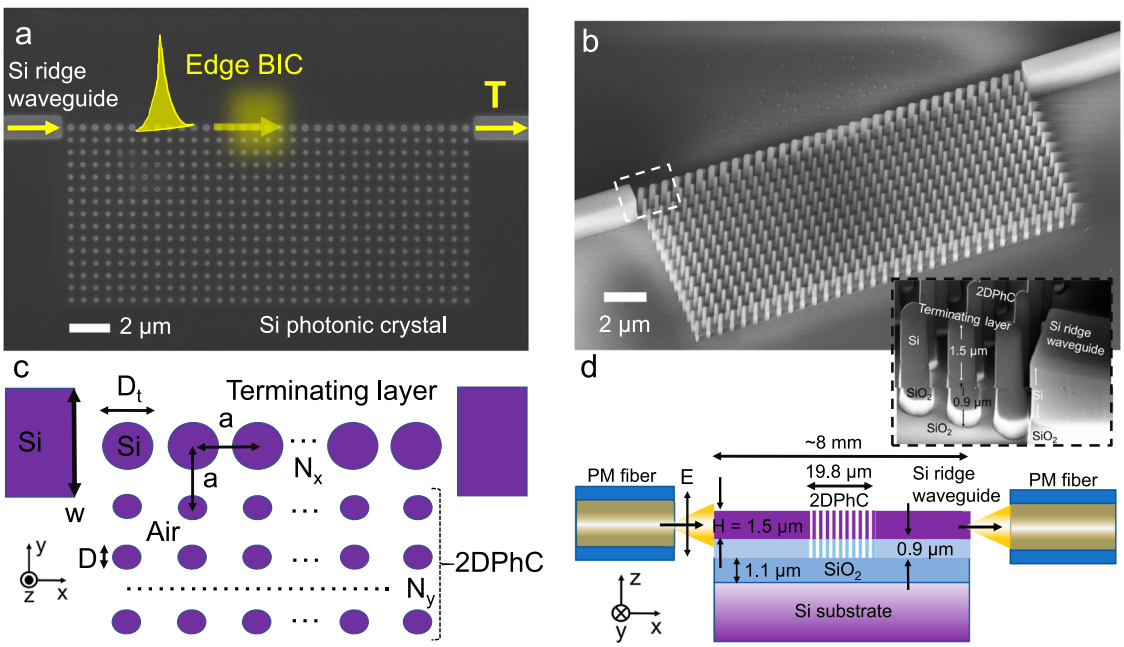

Fig. 1 | Truncated two-dimensional (2D) photonic crystal (PhC) structure, supporting edge bound state in the continuum (BIC). a Top and (**b**) birds-eye-view of scanning electron microscope (SEM) images of Si pillar PhCs and ridge waveguides after the deposition of 7.3 nm thick alumina film. The white dashed box corresponds to the inset of SEM image (black dashed box). Si pillars with 1.5 μm height lie on approximately 0.9 μm SiO_2 pillars. **c** The design of Si pillar PhC system and Si ridge waveguides on silicon on insulator (SOI) wafer (top view). The PhC structures under consideration have a lattice constant (period) of a = 600 nm, diameter D_t = 260 nm for the terminating layer and D = 160 nm for the rest of Si pillars, height H = 1.5 μm. The number of periods along the x- and y-axis is N_x = 33 and N_y = 15, including the terminating layer, giving the Si pillar PhC area of 19.8 × 9.0 μm. **d** Schematic illustration of the experimental setup for end-fire coupling to measure transmission spectra through 2DPhC (side view). Coupling and out-coupling of light is done by polarization-maintaining (PM) fibers. The width of both Si ridge waveguides is w = 1.0 μm, and their lengths are approximately 4 mm long for both input and out-coupling parts.

observation of edge BICs on truncated 2DPhCs. We also show that a slight change of the dielectric environment by a nanometer-thick dielectric layer deposited around Si pillars improves the Q-factor from 237 to 396 and shifts the quasi-BIC's resonance wavelength with 1.12 nm for every nanometer of the film thickness. This shows the option of the post-fabrication tuning of edge BIC modes and a strong potential for sensing applications in the detection of biomarkers.

Results

Numerical simulation

The 2DPhC structures under consideration have a lattice constant (period) of $a = 600$ nm, diameter $D_t = 270$ nm for the terminating layer, and $D = 160$ nm for the rest of Si pillars with height $H = 1.5$ μm. The Si pillars stand on top of SiO_2 pillars with 0.9 μm height created by under etch of SiO_2 layer (Fig. 1b and Supplementary Fig. S1) in order to make the mode confined within Si pillars due to effective refractive index contrast between Si pillars and SiO_2 pillars. Without the under etch of SiO_2, the quasi-BIC mode significantly leaks into SiO_2 layer and consequently, the transmission peak cannot be observed (Supplementary Figs. S2 and S3). The etch depth of 0.9 μm is chosen to suppress the leakage while not damaging the Si pillars themselves (Supplementary Fig. S4). The fabricated photonic crystal structure has $N_x = 33$ and $N_y = 15$ periods along x- and y-axis, respectively, covering 19.8 μm × 9.0 μm area (Fig. 1c). Note that the number N_y of 2DPhC periods along y-axis needs to be sufficient for the photonic crystal to function as a reflector, and $N_y = 5$ is enough as was validated in[46] (see also Supplementary Fig. S5). The 2DPhC area is in- and out-coupled by a pair of Si ridge waveguides with the same height of $H = 1.5$ μm and width $w = 1.0$ μm. These ridge waveguides stretch from the edge of the substrate and are used to inject broadband light into the 2DPhC area and to out-couple the guided modes to the polarization-maintaining (PM) single-mode fibers and further to the spectrometer (Fig. 1d). The 2DPhC and Si ridge waveguides are fabricated on a silicon on insulator (SOI) substrate with 2.0 μm thick silica (SiO_2) layer (Materials and methods).

We conducted numerical analysis to elucidate the nature of edge-bound states in the continuum, as shown in Fig. 2. Figure 2a shows the dispersion diagram of 2DPhC with lattice constant $a = 600$ nm and diameter of Si pillars $D = 160$ nm in air background. Such 2DPhC lattice has the bandgap extended for $\omega a/2\pi c = a/\lambda = 0.352–0.482$, corresponding to $\lambda = 1244–1704$ nm. The BIC appears within the photonic bandgap above the light line so that the mode in the terminating layer is reflected from the PhC side and the air semispace in a destructive manner. The edge BIC mode localized in the terminating layer propagates along the Γ-X direction of 2DPhC.

We also calculated the dispersion diagram for the 2DPhC with the terminating layer of Si pillars with diameter, $D_t = 270$, as shown in Fig. 2b. We locate a guided surface mode below the light line within the photonic bandgap, which transforms into a leaky mode above the light line (red dashed line in Fig. 2b). This leaky mode is the candidate to become a BIC mode, as predicted in the similar way in ref. 39. To locate the quasi-BIC mode, we analyzed the Q-factor of the leaky mode under question for the range of $k_x = 0.22–0.30$ (Fig. 2)c. A sharp increase of lifetime (Q-factor) that approaches infinity when the surface-parallel wavevector is near $k_x = 0.26325$. At this point B of Fig. 2c, the radiation of resonant mode is suppressed, while at the vicinity of point B (A and C points), fields are intensively leaking into the air.

Figure 2d shows the simulated transmission spectra through the 2DPhC with the terminating layer composed of a row of Si pillars with diameter $D_t = 270–280$ nm. Note that this wavelength interval $\lambda = 1400–1500$ nm is completely within the photonic bandgap ($\lambda = 1244–1704$ nm) that does not accept any light waves except for the edge BIC modes guided through the terminating layer. Therefore, we observe the transmission peak in low transmission background. The transmission peak red-shifts as the diameter becomes bigger. Moreover, the full-width at half maximum (FWHM) enlarges from FWHM = 10.2 nm of $D_t = 270$ nm to FWHM = 11.7 nm and 22.6 nm for $D_t = 275$ nm and 280 nm, respectively. The corresponding Q-factors degrade from $Q = 139$ ($D_t = 270$ nm) to 123 ($D_t = 275$ nm) and down to 64 ($D_t = 280$ nm) due to the broadening of the resonance peak. Thus, the diameter D_t can be optimized for the high-Q resonance edge BIC mode.

The field profiles in Fig. 2e exhibit a high concentration of the electric field around the terminating layer, similar to the edge BICs reported in ref. 39. We can also see that the field pattern repeats after approximately four periods of pillars. Thus, the effective wavelength λ_{eff} of this mode is $\lambda_{eff} \approx 4a = 2400$ nm for the vacuum wavelength of $\lambda = 1424$ nm, resulting in the normalized wavevector (in other words effective refractive index of the mode) of $N = 1424$ nm/2400 nm = 0.593. Note that here $N = \beta/k_0$ where β is propagation constant and k_0 is wavevector in vacuum, $k_0 = 2\pi/\lambda$. Since $N < 1$, this propagating mode exists above the light line of the dispersion spectra and leaks into the air, satisfying the condition of edge BICs. Moreover, $k_x = \beta a/2\pi = k_0 Na/2\pi = Na/\lambda \approx 0.25$, which corresponds to $k_x = 0.26325$ of point B in Fig. 2c and Fig. 5b of ref. 40. The normalized frequency of the edge BIC is $\omega a/2\pi c = a/\lambda = 600$ nm/1424 nm = 0.421. This is within the photonic bandgap of the 2DPhC ($\omega a/2\pi c = 0.352 – 0.482$ in Fig. 2a), also satisfying the condition for supporting edge BICs in 2DPhCs.

Measured transmission spectra. Silicon pillar PhC samples were fabricated by electron beam lithography and dry etching technique on silicon-on-insulator (SOI) wafers, as described in Materials and Methods. Here we stress that without the under etch of SiO_2 layer, we were unable to observe narrow transmission peak associated with the edge BICs due to the leakage of mode energy into substrate (see Supplementary Figs. S2 and S3), which may have prevented the demonstration of this edge BIC mode up to present. With the SiO_2 pedestal pillars underneath the Si pillars, the BIC modes are more confined within the Si pillars and observable transmission peaks are realized.

Figure 3 a shows measured transmission spectra for the 2DPhC samples (lattice constant $a = 600$ nm and Si pillar diameter $D = 160$ nm) in air with different diameters of the pillars in the terminating layer, D_t. We observe a transmission peak at $\lambda = 1424.0$ nm for the 2DPhC with $D_t = 260$ nm, which corresponds to the simulation of $D_t = 270$ nm case. This discrepancy in the optimal diameter D_t (Fig. 2d) between the simulation and experiment can be attributed to the imperfections in nanofabrication, such as the surface roughness of the pillars' side walls and rounding of top of pillars (see Supplementary Figs. S1 and S6). The transmission peak red-shifts (normalized frequency decreases as in Fig. 3b) for larger diameter $D_t = 264$ and 270 nm. The FWHM of the observed resonance of $D_t = 260$ nm is $FWHM = 6.0$ nm, which gives a quality factor of $Q = \lambda/FWHM = 237$, as summarized in Table 1. For $D_t = 264$ and 270 nm, the Q-factor decreases to $Q = \lambda/FWHM = 170$ and 160, respectively. The shape of resonance deforms for larger D_t, and as a result, the Q-factor degrades too (Fig. 3c), following the tendency observed in simulations.

Tunability and surface sensitivity measurement. Next, we investigate the tuning of the edge BIC resonance by a dielectric nanofilm conformally deposited on the 2DPhC structures with $D_t = 260$ nm and $D = 160$ nm. For that, alumina (Al_2O_3) layers with a refractive index of 1.61[47] around 1400–1500 nm wavelengths and thicknesses t_a between 2.5 to 7.3 nm are deposited on the sample's surface by the atomic layer deposition (ALD) technique (Materials and methods). Transmission measurements help to evaluate edge BIC's resonance tunability and surface sensitivity. Transmission spectra for samples with extra $t_a = 2.5$ nm, 4.7 nm, and 7.3 nm thick alumina coatings are shown in Fig. 4a. As summarized in Table 1, the transmission peak corresponding to the edge BIC mode red-shifts from 1424.0 nm to 1432.2 nm with a corresponding normalized frequency decrease (Fig. 4b) due to the increase of the local refractive index around Si

https://doi.org/10.1038/s41467-024-54929-0

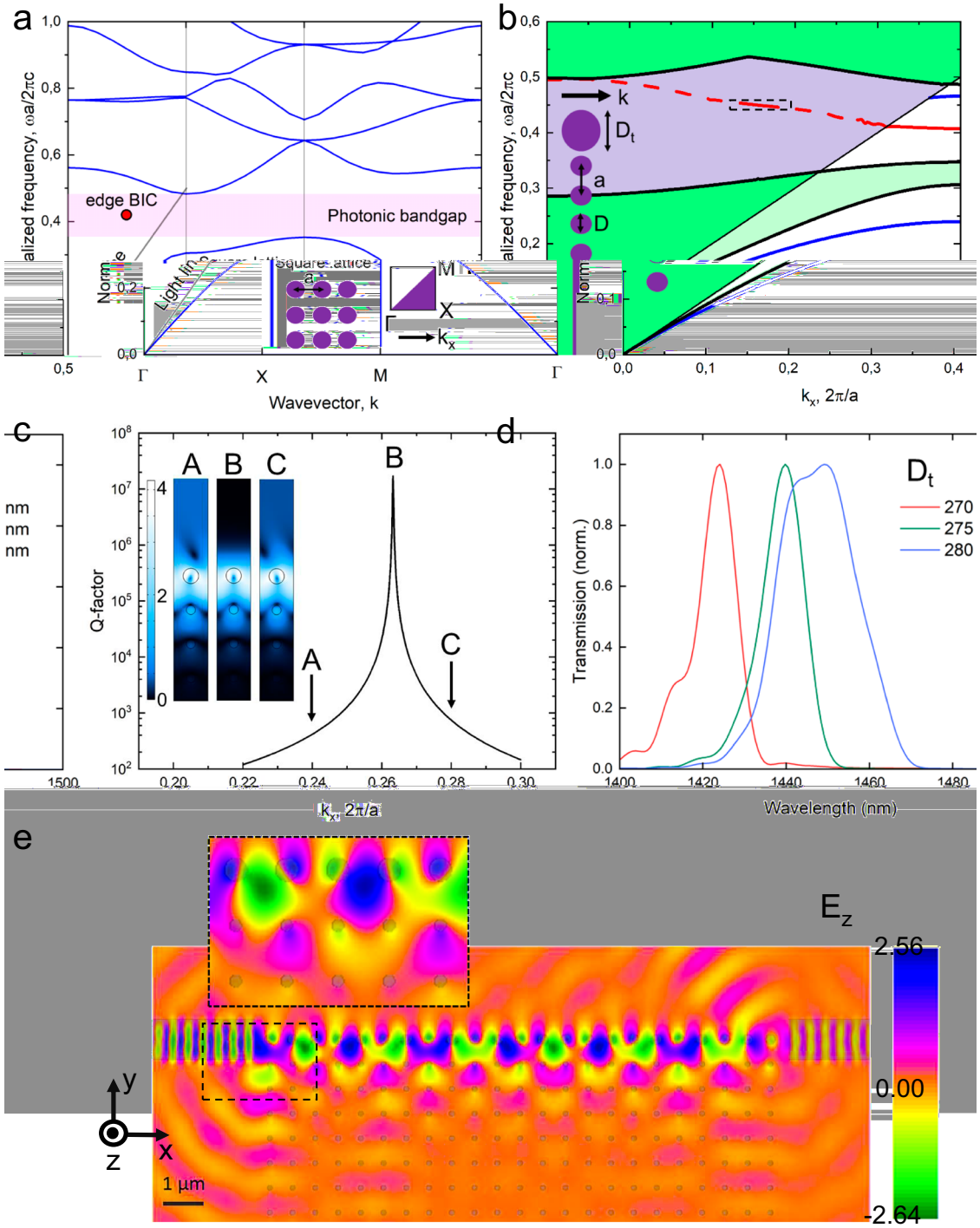

Fig. 2 | Simulation of edge-bound states in the continuum (BIC). a Simulated dispersion of two-dimensional photonic crystal (2DPhC) composed of Si pillars in a square lattice arrangement with air background, lattice constant a = 600 nm, diameter of D = 160 nm for transverse magnetic (TM) polarization (E_z parallel to Si pillars). The photonic bandgap extends from $\omega a/2\pi c = a/\lambda$ = 0.352 to 0.482 (λ = 1244–1704 nm). The position of the observed edge BIC at $\omega a/2\pi c = a/\lambda$ = 0.421 (λ = 1424 nm, k ~ 0.25) is marked by a red circle above the light line. **b** Dispersion for the 2DPhC with the terminating layer with D_t = 270 nm in air with the light line. The dashed square corresponds to the parameter space for (**c**) Quality factor of the leaky surface modes along the dashed red line in **b**. The inset shows the electric field profile of E_z at A: k_x = 0.24, B: k_x = 0.26325, and C: k_x = 0.28. **d** Simulated transmission spectra in 3D for three different diameters of terminating Si pillars, D_t = 270 nm (red), 275 nm (green), and 280 nm (blue), respectively. **e** E_z electric field profile of propagating mode (electric field parallel to Si pillars) through the terminating layer with Si pillar diameter D_t = 270 nm and D = 160 nm for 2DPhC for λ = 1424 nm. The inset shows the enlargement of dashed rectangular, showing one effective wavelength (period) of the edge BIC mode.

pillars. For t_a = 2.5 nm, the transmission peak with *FWHM* = 3.6 nm shifts to 1426.6 nm from the original position at 1424.0 nm with the reference sample without the alumina layer, giving increased $Q = \lambda/FWHM$ = 396, as plotted in Fig. 4c. For t_a = 4.7 nm and 7.3 nm, the Q-factor significantly drops to $Q = \lambda/FWHM$ = 270 and 247, respectively. This shows that we can realize fine post-tuning of the resonance and even improve the Q-factor from Q = 237 to 396 by depositing the dielectric nanofilm with the thickness of t_a = 2.5 nm.

https://doi.org/10.1038/s41467-024-54929-0

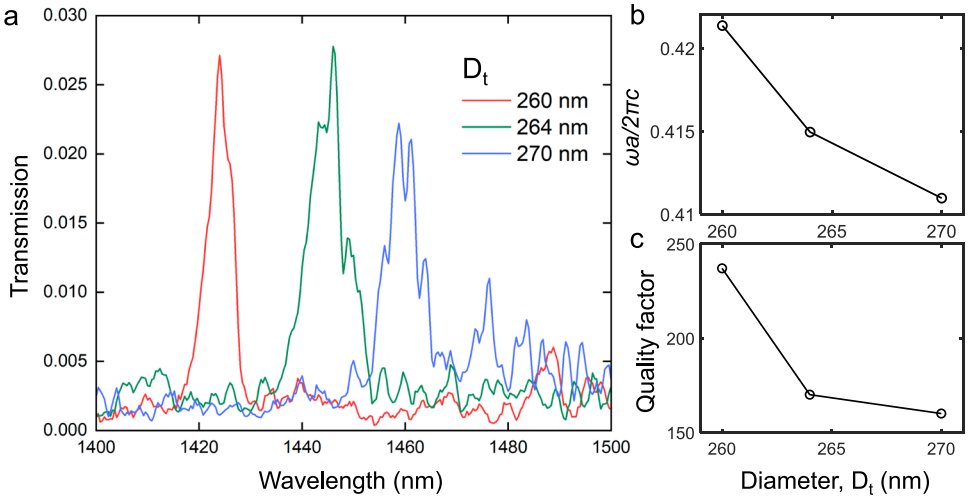

Fig. 3 | Observation of edge-bound states in the continuum (BIC). a Measured normalized transmission spectra through Si pillar photonic crystals (2DPhC) with three different diameters of terminating Si pillars, D_t = 260 nm (red), 264 nm (green), and 270 nm (blue), respectively. The 2DPhC samples have the period a = 600 nm, height H = 1.5 μm height, and D = 160 nm and the termination row of Si pillars with D_t = 260 -- 270 nm. **b** Normalized frequency, $\omega a/2\pi c$, and (c) quality factor of quasi-BIC modes for different diameters, D_t.

Table 1 | Summary of the measured performance of edge bound state in the continuum (BIC) supported on two-dimensional photonic crystal (2DPhC)

Diameter D_t [nm]	Wavelength λ [nm]	FWHM [nm]	Q-factor
260	1424.0	6.0	237
264	1446.0	8.5	170
270	1460.0	9.1	160
Alumina thickness t_a for D_t = 260 nm			
0	1424.0	6.0	237
2.5	1426.6	3.6	396
4.7	1429.1	5.3	270
7.3	1432.2	5.8	247

Si pillar diameter, D = 160 nm. *FWHM* full width at half-maximum.

This is a remarkable improvement of the Q-factor by 67 % compared with the reference structure without the alumina layer.

The pronounced wavelength shift induced by the nanometer-thick dielectric coating can be used for surface refractometric sensing to detect biomarkers. Surface sensitivity, a measure of wavelength shift, $\Delta\lambda$, for the thickness of the analyte layer, t_a is defined by[48–51]

$$S_s = \frac{\Delta\lambda[nm]}{t_a[nm]}. \quad (1)$$

In the case of refractometric sensing where analyte molecules form nanometer-thick film on sensor surface, the surface sensitivity is relevant. The resonance shift by an alumina nanofilm in linear fit gives a comfortable 1.12 nm variation with every nanometer of a binding layer thickness as shown in the inset of Fig. 4a. The observed surface sensitivity of 1.12 nm edge BICs shift for every nanometer thickness is comparable to 1.24–1.40 nm/nm sensitivity of guided-mode resonances supported in Si high-contrast grating structures with alumina layer as model analyte in air background[49,50]. To improve the surface sensitivity, the parameters of 2DPhC and terminating layer, especially their diameters, should be optimized to maximize the overlap of field and analyte[48].

Apart from the implication of potential applications for biosensing, the 2DPhC system supporting edge BICs may also find applications in temperature sensors and all-optical modulators for optical signals. The former application is due to the alteration of the ambient medium properties with temperature. The latter can be granted by the significant modulation strength of a system with powerful radiation. Recently, pronounced optical modulation by low fluence was demonstrated for Si metasurfaces that support collective modes such as guide mode resonances with comparable Q-factor (~170) for similar wavelengths (λ ~ 1380 nm)[52]. We anticipate that the edge BIC supported on Si-based 2DPhC and waveguides can be modulated by optical pulses at telecommunication wavelengths in a similar manner.

Discussion

A nanometer-thick oxide layer can shift the edge BIC resonance and improve its Q-factor. This suggests that the edge BIC resonance can be tuned by thin films conformally deposited by ALD as the post-fabrication tuning option. The ALD technique offers precise control of layer thickness and is advantageous for tuning edge BIC resonance. The maximum observed Q-factor of 396 with a 2.5 nm thick alumina layer increased from Q = 237 of the as-fabricated PhC is comparable to the reported numbers of Si-based metasurfaces supporting symmetry-protected BIC for the same wavelength region[10,11,23]. Further improvement of the Q factor can be realized in two ways. The first option is to increase the number of periods along the x-direction, N_x, since a pure BIC with an infinitely high Q-factor assumes an infinite number of periods. Thus, more periods result in higher Q-factor[53]. The other way is to reduce the fabrication imperfection, such as side wall roughness of Si pillars and tapering, which increases scattering loss and results in the degradation of the resonance quality.

In summary, we demonstrate the observation of unique type of FP-BIC modes supported at the edge of truncated 2DPhC composed of Si pillars in square lattice structures for a near-IR wavelength range from 1400 to 1500 nm. The edge BICs are supported by the Si pillars of larger diameter in the terminating layer than that of host 2DPhC. The Q-factor and resonance wavelength can be tuned by a nanometer-thick alumina layer conformally deposited by ALD. The fine-tuning of quasi-BIC results in an improved Q-factor by over 60 % and a red-shift of the resonance wavelength. These features can be used for surface sensing and refractometric sensing in the detection of biomarkers.

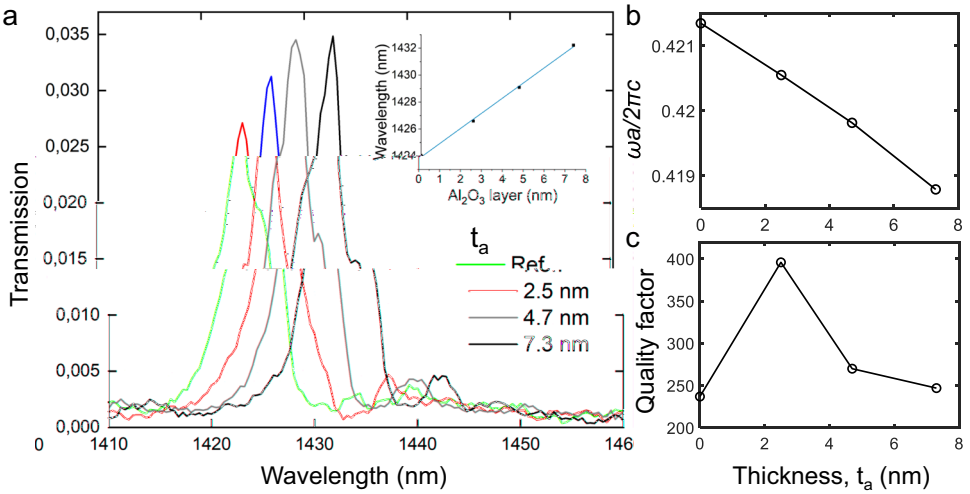

Fig. 4 | Surface sensitivity and tunability of quasi-bound state in the continuum (BIC). a Transmission spectra of two-dimensional (2D) Si pillar photonic crystals (PhCs) with different alumina thicknesses, t_a = 0 nm as reference (Ref. red), 2.5 nm (blue), 4.7 nm (gray), and 7.3 (black), for D_t = 260 nm and D = 160 nm. The inset shows the surface sensitivity S_s as the resulting resonance shift in wavelength for the thickness of alumina layers deposited on the samples. **b** Resonance in normalized frequency, $\omega a/2\pi c$, and (**c**) quality factor in terms of deposited alumina film thickness, t_a.

Methods

Theoretical analysis

The photonic band diagram in 2D (Fig. 2a) was simulated by MIT Photonic-Bands (MPB) software package[54]. The band diagram and Q-factors in terms of wavevector (Fig. 2b and c) were calculated by finite element method with COMSOL (COMSOL, Inc). The transmission spectra (Fig. 2d, Supplementary Figs. S2 and S5) and electrical field profile (Fig. 2e) were calculated, using Lumerical (Lumerical FDTD solutions from Lumerical Inc.) software based on finite-difference time-domain (FDTD) method with mesh size of 2 nm. The refractive indices of Si and SiO_2 are 3.48 and 1.46, respectively. Note that the transmission spectra in Fig. 2d is normalized to the maximum one.

Sample fabrication

Truncated photonic crystal structures were fabricated by electron beam lithography and reactive ion etching (RIE) on an SOI (silicon on insulator) wafer with a 1.5 μm silicon device layer on top of a buried, 2 μm thick, silica layer (Supplementary Fig. S7). The wafers were acquired from Siegert Wafer GmbH (Germany). The device layer consists of <100 > crystalline p-type silicon with a specified resistivity of 1-5 Ohm-cm. The wafer was prepared for electron beam exposure by spin-coating a 180 nm layer of CSAR positive resist (AR-P 6200, Allresist GmbH, Germany) followed by thermal evaporation of a 20 nm aluminum discharge layer. The desired pattern was exposed using a JEOL JBX-9500FS electron beam lithography system with a dose of 350 $\mu C/cm^2$. The discharge layer was stripped in TMAH developer, AZ 726 MIF (Merck, Germany), subsequently developed using developer, AR 600-546 (Allresist GmbH, Germany) for 90 seconds. A new 20 nm aluminum layer was deposited using e-beam evaporation. A lift-off process was carried out (Microposit Remover 1165) to remove the CSAR resist, leaving the aluminum layer with the desired pattern as a mask for the subsequent dry etch.

RIE using SPTS-Pegasus etcher was done using a single processing step with a mix of etching gas (SF_6 at 44 sccm) and passivation gas (C_4F_8 at 77 sccm). The etch process lasted for 5–6 minutes with a coil power of 1000 W and a platen power of 20 W until the buried oxide was reached and the silicon device layer was fully removed. The processing parameters were then changed (40 sccm C_4F_8, 5 sccm O_2, coil power 1100 W, platen power 180 W) in order to etch into the oxide for 2 min by STS-MESC Multiplex ICP etcher, giving an etch depth of approximately 900 nm (Supplementary Fig. S1). Afterwards, the remaining aluminum mask was removed using TMAH developer.

Alumina layers of t_a = 2.5, 4.7, and 7.3 nm were conformally deposited on samples by the atomic layer deposition (ALD) technique by 25, 50, and 75 cycles, respectively (Fig. 4). Their thickness is measured by an ellipsometer on a flat Si substrate deposited at the same time as 2DPhC samples.

Transmission measurement

The experimental setup is shown in Fig. S8 of Supplementary Information. Supercontinuum light from the broadband laser (SuperK; NKT Photonics A/S, Birkerød, Denmark, emission wavelength: λ = 350–2400 nm) was coupled to the Si ridge waveguide at the cleaved edge of Si chip by end-fire coupling through a single mode polarization maintaining (PM) fiber. The transmitted light are out-coupled from the other end of Si ridge waveguide through another single-mode PM fiber and detected by the optical spectrum analyser (OSA, Ando AQ-6315E; Yokogawa Electric Corp. Tokyo, Japan, detection wavelength range: λ = 500–1750 nm) with the wavelength steps of 0.4 nm for Figs. 3, 4 and 0.6 nm for Supplementary Fig. S3, respectively. The baseline transmission was taken from the transmission spectrum through the Si waveguide with the same length but without the photonic crystal part, which was then used to normalize the measured transmission from the samples in Figs. 3, 4, and Supplementary Fig. S3.

Data availability

The source plots for Figs. 2–4 and Supporting Information generated in this study have been deposited in the Figshare database under accession code [https://doi.org/10.6084/m9.figshare.27331821].

References

1. Marinica, D. C., Borisov, A. G. & Shabanov, S. V. Bound states in the continuum in photonics. *Phys. Rev. Lett.* **100**, 183902 (2008).
2. Plotnik, Y. et al. Experimental Observation of Optical Bound States in the Continuum. *Phys. Rev. Lett.* **107**, 183901 (2011).
3. Hsu, C. W. et al. Observation of trapped light within the radiation continuum. *Nature* **499**, 188–191 (2013).
4. Hsu, C. W., Zhen, B., Stone, A. D., Joannopoulos, J. D. & Soljacic, M. Bound states in the continuum. *Nat. Rev. Mater.* **1**, 16048 (2016).

5. Joseph, S., Pandey, S., Sarkar, S. & Joseph, J. Bound states in the continuum in resonant nanostructures: An overview of engineered materials for tailored applications. *Nanophotonics* **10**, 4175–4207 (2021).
6. Xu, G. et al. Recent Advances and Perspective of Photonic Bound States in the Continuum. *Ultrafast Sci.* **3**, 0033 (2023).
7. Kodigala, A. et al. Lasing action from photonic bound states in continuum. *Nature* **541**, 196–199 (2017).
8. Wu, M. et al. Room-Temperature Lasing in Colloidal Nanoplatelets via Mie-Resonant Bound States in the Continuum. *Nano Lett.* **20**, 6005–6011 (2020).
9. Liu, Z. et al. High- Q Quasibound States in the Continuum for Nonlinear Metasurfaces. *Phys. Rev. Lett.* **123**, 253901 (2019).
10. Koshelev, K. et al. Nonlinear Metasurfaces Governed by Bound States in the Continuum. *ACS Photonics* **6**, 1639–1644 (2019).
11. Xu, L. et al. Dynamic Nonlinear Image Tuning through Magnetic Dipole Quasi-BIC Ultrathin Resonators. *Adv. Sci.* **6**, 1802119 (2019).
12. Bernhardt, N. et al. Quasi-BIC Resonant Enhancement of Second-Harmonic Generation in WS2Monolayers. *Nano Lett.* **20**, 5309–5314 (2020).
13. Sinev, I. S. et al. Observation of Ultrafast Self-Action Effects in Quasi-BIC Resonant Metasurfaces. *Nano Lett.* **21**, 8848–8855 (2021).
14. Okhlopkov, K. I. et al. Tailoring Third-Harmonic Diffraction Efficiency by Hybrid Modes in High-Q Metasurfaces. *Nano Lett.* **21**, 10438–10445 (2021).
15. Abdelraouf, O. A. M., Anthur, A. P., Wang, X. R., Wang, Q. J. & Liu, H. Modal Phase-Matched Bound States in the Continuum for Enhancing Third Harmonic Generation of Deep Ultraviolet Emission. *ACS Nano* **18**, 4388–4397 (2024).
16. Sun, X. et al. Manipulating Dual Bound States in the Continuum for Efficient Spatial Light Modulator. *Nano Lett.* **22**, 9982–9989 (2022).
17. Romano, S. et al. Label-free sensing of ultralow-weight molecules with all-dielectric metasurfaces supporting bound states in the continuum. *Photonics Res.* **6**, 726 (2018).
18. Tittl, A. et al. Imaging-based molecular barcoding with pixelated dielectric metasurfaces. *Science* **360**, 1105–1109 (2018).
19. Yesilkoy, F. et al. Ultrasensitive hyperspectral imaging and biodetection enabled by dielectric metasurfaces. *Nat. Photonics* **13**, 390–396 (2019).
20. Wang, J. et al. All-Dielectric Crescent Metasurface Sensor Driven by Bound States in the Continuum. *Adv. Funct. Mater.* **31**, 2104652 (2021).
21. Schiattarella, C. et al. High-Q photonic aptasensor based on avoided crossing bound states in the continuum and trace detection of ochratoxin A. *Biosens. Bioelectron. X* **12**, 100262 (2022).
22. Jacobsen, R. E., Krasnok, A., Arslanagic, S., Lavrinenko, A. V. & Alu, A. Boundary-Induced Embedded Eigenstate in a Single Resonator for Advanced Sensing. *ACS Photonics* **9**, 1936–1943 (2022).
23. Watanabe, K. & Iwanaga, M. Nanogap enhancement of the refractometric sensitivity at quasi-bound states in the continuum in all-dielectric metasurfaces. *Nanophotonics* **12**, 99–109 (2023).
24. Zhao, H. et al. Large-area silicon photonic crystal supporting bound states in the continuum and optical sensing formed by nanoimprint lithography. *Nanoscale Adv.* **5**, 1291–1298 (2023).
25. Loon, T. et al. Refractive index sensing using quasi-bound states in the continuum in silicon metasurfaces. *Opt. Express* **32**, 14289 (2024).
26. Beliaev, L. Y., Takayama, O. & Xiao, S. Effectively detecting cardiac myoglobin by use of bound states in the continuum in silicon nitride gratings. *J. Appl. Phys.* **135**, 223101 (2024).
27. Beliaev, L., Takayama, O. & Lavrinenko, A. Subwavelength periodic dielectric nanostructures for biochemical sensing. In: Armani, A., Chalyan, T., Sampson, D.D. (eds.) Biophotonics and Biosensing: From Fundamental Research to Clinical Trials Through Advances of Signal and Image Processing, 1st edn., pp. 157–187. Elsevier, Amsterdam https://doi.org/10.1117/3.100303.ch5 (2024).
28. Romano, S. et al. Ultrasensitive surface refractive index imaging based on quasi-bound states in the continuum. *ACS Nano* **14**, 15417–15427 (2020).
29. Schiattarella, C. et al. Directive giant upconversion by supercritical bound states in the continuum. *Nature* **626**, 765–771 (2024).
30. Sadrieva, Z. F. et al. Transition from Optical Bound States in the Continuum to Leaky Resonances: Role of Substrate and Roughness. *ACS Photonics* **4**, 723–727 (2017).
31. Murai, S. et al. Engineering Bound States in the Continuum at Telecom Wavelengths with Non-Bravais Lattices. *Laser Photonics Rev.* **16**, 2100661 (2022).
32. Liu, Z. et al. Phase Interrogation Sensor Based on All-Dielectric BIC Metasurface. *Nano Lett.* **23**, 10441–10448 (2023).
33. Huang, L. et al. Realizing Ultrahigh-Q Resonances Through Harnessing Symmetry-Protected Bound States in the Continuum. *Adv. Funct. Mater.* **34**, 2309982 (2024).
34. Gomis-bresco, J., Artigas, D. & Torner, L. Anisotropy-induced photonic bound states in the continuum. *Nat. Photonics* **11**, 232–236 (2017).
35. Mukherjee, S., Artigas, D. & Torner, L. Surface bound states in the continuum in Dyakonov structures. *Phys. Rev. B* **105**, 201406 (2022).
36. Pitruzzello, G. & Krauss, T. F. Photonic crystal resonances for sensing and imaging. *J. Opt. (U. Kingd.)* **20**, 073004 (2018).
37. Vertchenko, L., DeVault, C., Malureanu, R., Mazur, E. & Lavrinenko, A. Near-Zero Index Photonic Crystals with Directive Bound States in the Continuum. *Laser Photonics Rev.* **15**, 2000559 (2021).
38. Zhao, H. et al. Large-Area Silicon Photonic Crystal Supporting Bound States in the Continuum and optical sensing Formed by Nanoimprint Lithography. *Nanoscale Adv.* **5**, 1291–1298 (2023).
39. Wei Hsu, C. et al. Bloch surface eigenstates within the radiation continuum. *Light. Sci. Appl.* **2**, 84 (2013).
40. Hu, Z. & Lu, Y. Y. Propagating bound states in the continuum at the surface of a photonic crystal. *J. Opt. Soc. Am. B* **34**, 1878 (2017).
41. Bulgakov, E. N. & Sadreev, A. F. Bloch bound states in the radiation continuum in a periodic array of dielectric rods. *Phys. Rev. A -. Mol. Opt. Phys.* **90**, 053801 (2014).
42. Hu, P. et al. Bound states in the continuum based on the total internal reflection of Bloch waves. *Natl Sci. Rev.* **10**, 043 (2023).
43. Bykov, D. A., Bezus, E. A. & Doskolovich, L. L. Bound states in the continuum and strong phase resonances in integrated gires-tournois interferometer. *Nanophotonics* **9**, 83–92 (2020).
44. Nabol, S. V., Pankin, P. S., Maksimov, D. N. & Timofeev, I. V. Fabry-Perot bound states in the continuum in an anisotropic photonic crystal. *Phys. Rev. B* **106**, 245403 (2022).
45. Weimann, S. et al. Compact surface fano states embedded in the continuum of waveguide arrays. *Phys. Rev. Lett.* **111**, 240403 (2013).
46. Lavrinenko, A. et al. Comprehensive FDTD modelling of photonic crystal waveguide components. *Opt. Express* **12**, 234 (2004).
47. Zhukovsky, S. V. et al. Experimental Demonstration of Effective Medium Approximation Breakdown in Deeply Subwavelength All-Dielectric Multilayers. *Phys. Rev. Lett.* **115**, 177402 (2015).
48. Finco, G. et al. Guided-mode resonance on pedestal and half-buried high-contrast gratings for biosensing applications. *Nanophotonics* **10**, 4289–4296 (2021).
49. Beliaev, L. Y. et al. Pedestal High-Contrast Gratings for Biosensing. *Nanomaterials* **12**, 1748 (2022).
50. Beliaev, L. Y. et al. Optical Biosensors Based on Nanostructured Silicon High-Contrast Gratings for Myoglobin Detection. *ACS Appl. Nano Mater.* **6**, 12364–12371 (2023).
51. Zhou, Y. et al. Asymmetric tetramer metasurface sensor governed by quasi-bound states in the continuum. *Nanophotonics* **12**, 1295–1307 (2023).

52. Tognazzi, A., Franceschini, P., Sergaeva, O., Carletti, L. & Alessandri, I. Giant photoinduced reflectivity modulation of nonlocal resonances in silicon metasurfaces. *Adv. Photonics* **5**, 066006 (2023).
53. Taghizadeh, A. & Chung, I. S. Quasi bound states in the continuum with few unit cells of photonic crystal slab. *Appl. Phys. Lett.* **111**, 031114 (2017).
54. Johnson, S. G. & Joannopoulos, J. D. Block-iterative frequency-domain methods for Maxwell's equations in a planewave basis. *Opt. Express* **8**, 173–190 (2001).

Acknowledgements

This work was supported by the European Union's Horizon 2020 research and innovation programme under the FETOPEN (grant agreement number 964808) "Continuous two-dimensional Stretch monitoring of fresh tissue Biopsies (StretchBio)", the Danish National Research Foundation through NanoPhoton - Center for Nanophotonics (grant number DNRF147), and Villum Fonden, Villum Investigator Project (grant number 00037822) "Table-Top Synchrotrons". The authors would like to acknowledge the support from the Danish National Center for Micro- and Nanofabrication (DTU Nanolab). M. N. would like to thank Sergei Lepeshov for valuable comments.

Author contributions

R.S. performed modeling and theoretical analysis of the structures, and conducted optical characterization of samples. C.V.B. fabricated the samples. M.N. performed part of modeling and theoretical analysis of the structures. R.S. and E.L.A performed part of sample fabrication. R.M. and W.E.S. contributed to the discussion of results and manuscript editing. A.V.L. participated in the discussion of results and manuscript writing. O.T. conceived the idea, wrote manuscript, and supervised the work. All authors have given approval to the final version of the manuscript.

Competing interests

The authors declare no competing interests.

Additional information

Supplementary information The online version contains supplementary material available at https://doi.org/10.1038/s41467-024-54929-0.

Correspondence and requests for materials should be addressed to Osamu Takayama.

Peer review information *Nature Communications* thanks the anonymous reviewer(s) for their contribution to the peer review of this work. A peer review file is available.